

1      **This Manuscript is Currently Submitted and Under Revision.**

2      **Title: Spatial Transcriptomics Reveals Inflammation and Trans-differentiation States of**  
3      **Acute Myeloid Leukemia in Extramedullary and Medullary Tissues**

5      **Short Title: Spatial Transcriptomics in Acute Myeloid Leukemia**

7      Enes Dasdemir<sup>1,2</sup>, Ivo Veletic<sup>1</sup>, Christopher P. Ly<sup>1</sup>, Andres E. Quesada<sup>3</sup>, Fatima Z. Jelloul<sup>3</sup>,  
8      Pamela Borges<sup>2</sup>, Sreyashi Basu<sup>4</sup>, Sonali Jindal<sup>4</sup>, Zhiqiang Wang<sup>4</sup>, Alexander Lazar<sup>5</sup>, Khalida M.  
9      Wani<sup>5</sup>, Dinler A. Antunes<sup>2</sup>, Patrick K. Reville<sup>1</sup>, Preethi H. Gunaratne<sup>2</sup>, Robert J. Tower<sup>7</sup>,  
10     Padmanee Sharma<sup>4,6</sup>, Hussein A. Abbas<sup>1,8\*</sup>

- 11
- 12     1. Department of Leukemia, Division of Cancer Medicine, The University of Texas MD  
13     Anderson Cancer Center, Houston, TX, USA.
  - 14     2. Department of Biology and Biochemistry, University of Houston, Houston, TX, USA.
  - 15     3. Department of Hematopathology, Division of Cancer Medicine, The University of Texas  
16     MD Anderson Cancer Center, Houston, TX, USA.
  - 17     4. Immunotherapy Platform, James P. Allison Institute, The University of Texas MD  
18     Anderson Cancer Center, Houston, TX, USA.
  - 19     5. Department of Pathology, Division of Pathology/Lab Medicine, The University of Texas  
20     MD Anderson Cancer Center, Houston, TX, USA.
  - 21     6. Department of Genitourinary Medical Oncology, Division of Cancer Medicine, The  
22     University of Texas MD Anderson Cancer Center, Houston, TX, USA.
  - 23     7. Department of Surgery, University of Texas Southwestern Medical Center, Dallas, TX,  
24     USA
  - 25     8. Department of Genomic Medicine, Division of Cancer Medicine, The University of Texas  
26     MD Anderson Cancer Center, Houston, TX, USA.

28      **\*Corresponding author**

29      Hussein A. Abbas, MD, PhD  
30      Department of Leukemia  
31      Department of Genomic Medicine  
32      M D Anderson Cancer Center  
33      Houston, TX  
34      [Habbas@mdanderson.org](mailto:Habbas@mdanderson.org)

36      **Abstract**

38      Acute myeloid leukemia (AML) is a heterogeneous disease of the bone marrow (medullary) but  
39      can also involve extramedullary tissues. While single cell dynamics of AML in suspension are  
40      previously explored, a comprehensive spatial transcriptomic assessment in AML remain  
41      underexplored. Here, we used Visium spatial transcriptomics to resolve medullary and  
42      extramedullary AML environments. We reveal spatial co-localization of monocytes and  
43      granulocyte-monocyte progenitors with leukemic populations in the bone marrow, sharing  
44      molecular signatures with extramedullary sites. Cell-cell communication via the CXCL12-CXCR4  
45      axis correlated with PI3K/AKT/mTOR signaling in high inflammatory niches. Trans-differentiation

46 states were concentrated in AML-infiltrated regions, with committed-like AML populations present  
47 in inflammatory niches and away from the trabeculae, while primitive-like AML cells localized near  
48 the endosteal niche. We validated these findings in GeoMx-based Digital Spatial profiling (DSP).  
49 Our study applied multimodal spatial transcriptomic approaches to characterize the spatial  
50 hierarchy and microenvironmental dynamics of AML differentiation states. We also demonstrated  
51 the feasibility of applying Visium-based spatial transcriptomics in decalcified bone tissues.

52

### 53 **Introduction**

54

55 Acute myeloid leukemia (AML) is a clonal disorder characterized by the presence of immature  
56 blasts and arrested differentiation.<sup>1</sup> Even with the advent of new treatments<sup>2,3</sup>, the overall five-  
57 year survival rate remains dismally low at around 30%.<sup>4</sup> Clinical manifestations of AML are largely  
58 attributed to the ability of myeloid neoplastic cells to impair hematopoiesis and disrupt the immune  
59 system function in the bone marrow (BM).<sup>5,6</sup> However, the traditionally view of AML as a BM-  
60 centric illness, fails to encapsulate its ability to infiltrate extramedullary (EM) tissues, a condition  
61 also known as myeloid sarcoma (MS), which occurs in up to 22% of AML patients.<sup>7</sup> Interestingly,  
62 some AML patients may present with isolated MS without BM involvement.<sup>8</sup> These EM  
63 manifestations underscore the disease's insidious capacity for dissemination beyond the BM and  
64 its adaptability to extra-osseous sites. A thorough investigation of AML's spatial interactions may  
65 reveal the distinct behavior of AML cells in various microenvironments and aid in understanding  
66 its adaptability to difference niches.

67

68 Recent advances in high-throughput single-cell genomics and transcriptomics have improved our  
69 ability to molecularly dissect cellular identities, unravel gene regulatory networks, and  
70 characterize cellular states and their interactions within the BM and tumor microenvironment.<sup>9–11</sup>  
71 However, due to tissue dissociation, these approaches result in the loss of spatial context, which  
72 is crucial for preserving microenvironmental information.<sup>12</sup> While spatial proteomic analysis has  
73 provided valuable perspectives on mechanisms of AML to evade immune surveillance<sup>13,14</sup> and  
74 revealed subcellular compartments in AML cells,<sup>15</sup> spatial proteomics can be constrained by a  
75 predetermined, targeted approach, limiting its breadth to a fixed set of proteins and favoring  
76 validation over novel discovery. In contrast, spatial transcriptomics (ST) has emerged as an  
77 investigative tool, capturing a vast array of genes without bias, and facilitating the discovery of  
78 biological pathways, molecular profiling, and cellular interactions.<sup>16–19</sup>

79

80 Within the array of spatial transcriptomic methodologies<sup>20,21</sup>, the Visium pipeline from 10X  
81 Genomics offers comprehensive transcriptome profiling, though its resolution is confined to spots  
82 of 55 µm, which restricts its application for single-cell transcriptomics. Nonetheless, it supports  
83 high-throughput RNA profiling and facilitates the integration with single-cell RNA sequencing  
84 (scRNA-seq) data from cells in suspension, whereas the analysis is enhanced through  
85 deconvolution techniques.<sup>22–27</sup> While the application of Visium-based ST in solid tumors is on the  
86 rise,<sup>28–32</sup> to the best of our knowledge at the time of writing this manuscript, its potential in BM  
87 diseases and specifically AML, remains less explored. Also, the rigorous decalcification required  
88 for processing and sectioning of BM specimens may compromise RNA integrity, coupled with the

89 perception of BM diseases as ‘liquid’ cancers lacking a defined tissue architecture, may have  
90 impeded advancements in this area.

91  
92 In this study, we performed Visium array-based ST using two different chemistry versions in BM  
93 and EM leukemias from two AML patients with tissues collected at the time of diagnosis. We  
94 investigated the cellular composition across different BM and EM samples, highlighting spatial  
95 heterogeneity. By adapting a median absolute deviation (MAD)-based spot-filtering approach for  
96 unique structure metrics and using BM suspension scRNA-seq reference from 16 samples (n=9  
97 healthy and n=7 AML) for spatial deconvolution, we provided a spatial map of medullary and  
98 extramedullary leukemia. Our findings reveal the connection between leukemic populations via  
99 the CXCL12-CXCR4 axis and the spatial patterns of its downstream targets across the BM-EM  
100 axis. Additionally, we showed the involvement of inflammatory and endosteal BM niches in the  
101 maturation states of AML populations. We then validated our findings using digital spatial profiling  
102 (DSP) in an independent group of AML patients to better delineate the spatial relationship of AML  
103 hierarchy to bone structures.

104

## 105 **Materials and methods**

106

107 This study adheres to the principles outlined in the Declaration of Helsinki. All uses of human  
108 material were conducted following written informed consent.

109

## 110 **Sample preparation**

111

112 BM and EM tissue biopsies were routinely collected before treatment initiation from 2 patients  
113 with newly diagnosed AML. The samples were formalin fixed, and BM samples were decalcified  
114 using 10% formic acid. Following fixation and decalcification, the samples were embedded in  
115 paraffin and stored at room temperature before they were cut into 4- $\mu$ m sections.

116

## 117 **Clinical immunohistochemistry**

118

119 For immunohistochemistry (IHC) staining, tissue sections were first deparaffinized and rehydrated  
120 in xylene followed by graded alcohols. Endogenous peroxidase activity was blocked using 3%  
121 hydrogen peroxide. Heat-induced antigen retrieval was performed in a citrate buffer at 95°C.  
122 Following a protein block with 2.5% goat serum, primary antibodies specific to relevant markers  
123 (e.g., CD11c, MPO, and CD3e) were applied to the sections and incubated for 1 hour. The primary  
124 antibodies were detected using a horseradish peroxidase-conjugated secondary antibody and a  
125 DAB substrate. Nuclei were counterstained with hematoxylin. Finally, the stained slides were  
126 dehydrated and mounted with coverslips.

127

## 128 **GeoMx Digital Spatial Profiling**

129

130 An 8x8 core tissue microarray was created from 12 formalin-fixed, paraffin-embedded bone core  
131 biopsy samples. Nine cores were selected for DSP characterization. Two cores (areas of

illumination [AOI] 1-3) were not included in the present study due to a diagnosis of M6 (acute erythroid) leukemia. GeoMx sample preparation was performed as described previously.<sup>88</sup> For 3 cores, region of interest (ROIs) were selected both adjacent to and at least 200 µm distal from bone structures to characterize the tumor microenvironment proximal and distal to the bone. The tissue microarray was then stained with anti-CD68 (KP1) antibody, anti-CD34 (QBend/10) antibody, and SYTO13 nuclear stain to identify AML-enriched areas and to segment the ROIs into CD68, CD34, and non-myeloid areas of illumination (AOIs). Oligonucleotide barcodes attached to *in situ* hybridization probes from the GeoMx whole transcriptome atlas WTA were used to capture RNA expression for over 18,000 genes. The barcodes were cleaved using a UV laser to spatially capture expression in each AOI, then quantified.

142

RNA data underwent quality assurance using the GeomxTools R package.<sup>89</sup> In brief probes under the limit of quantification (defined as 2 standard deviations above the geometric mean of the negative control probes for each segment) in were removed from analysis. Probe counts were then normalized using quartile 3 (Q3) normalization and log transformed as recommended by NanoString.<sup>88</sup> RNA samples from myeloid AOIs were deconvolved *in silico* with CIBERSORTx<sup>90</sup> using our generated cell types as the reference. To simplify analysis, common myeloid progenitor/lymphoid-primed multipotent progenitor-like and HSC-like categories were combined into primitive-like, basophil-like, dendritic cell-like, and monocyte-like were combined into committed-like, and lymphoid-like and common lymphoid progenitor-like were combined into lymphoid-like. Differences in cell type abundance by proximity to bone were compared using a paired two-sample t-test. All analysis was performed using the R statistical language version 4.3.0.

155

## 156 Visium ST experimental methods

157

Formalin-fixed paraffin-embedded (FFPE) tissue from 2 BM and 2 EM leukemia samples were used for spatial transcriptomics analysis. Samples were paraffin-embedded and serially sectioned (thickness 4 µm). FFPE samples were tested for RNA quality with a DV<sub>200</sub> measurement by 2100 Electrophoresis Bioanalyzer (Agilent; G2939BA). The samples were then processed according to the standard Visium-Cytassist Spatial Gene Expression protocol (CytAssist-enabled) for the v2 assay using Visium CytAssist Reagent Kit, and standard Visium Spatial Gene Expression protocol (Direct placement) for the v1 assay (10X Genomics). The samples to be used for the v1 assay were directly placed on the Visium Spatial Gene Expression slide, which contains spatially unique capture oligonucleotides with 6.5 x 6.5 mm capture area. The samples for the v2 assays were placed on a standard glass slide and processed through Visium CytAssist and transferred to Visium' 11 x 11 mm capture area slide.

169

Libraries were cleaned up using SPRI select reagent and quantified using the High Sensitivity DNA Kit run on the Agilent 2100 Bioanalyzer, as well as the KAPA Library Quantification Kit for the Illumina platform (Roche, 7959362001) run on LightCycler 480. The library pool was quantified on the Bioanalyzer and with quantitative polymerase chain reaction and was sequenced using Illumina NovaSeq 6000.

175

176 **Visium ST analysis workflow**177 **Raw read processing with SpaceRanger**

178

179 Processing of spatial data was conducted using the SpaceRanger (version 2.0) software suite  
 180 provided by 10X Genomics. For datasets derived from the Visium v1, raw base call (BCL) files  
 181 were generated. These BCL files were transformed into FASTQ format utilizing the mkfastq  
 182 function of the SpaceRanger. Datasets obtained from the Visium v2 were directly procured in  
 183 FASTQ format. These FASTQ files were then aligned to the human reference genome GRCh38,  
 184 sourced from 10X Genomics, utilizing the count function to map barcoded spots to individual  
 185 slides. The analytical evaluation involved examining metric summaries and web summary files for  
 186 each sample to facilitate comparative analysis. To evaluate the performance of each sample,  
 187 median values of the number of oligonucleotides and genes metrics were calculated.

188

189 **Pathology Annotation**

190

191 H&E-stained slides were digitized (40x) using the Aperio from Leica Biosystems. Clinical IHC-  
 192 stained slides were scanned at 40x using an Akoya Biosciences Vectra Polaris automated  
 193 quantitative pathology imaging system. Images were annotated by expert pathologists using the  
 194 Aperio ImageScope pathology slide viewing software (version 12.4.6). Spots that fall in these  
 195 annotated regions were identified using the Loupe Browser. The spot barcodes and annotations  
 196 were exported as a CSV file and added to the metadata of our Seurat objects. These annotations  
 197 were then visualized using the *SpatialDimPlot* function.

198

199 **Spatial MAD**

200

201 Read count matrices and spatial informations were loaded using the *Load10X\_Spatial* function  
 202 from the *Seurat* R package (version 5.0.3). Mitochondrial content was assessed using the  
 203 *PercentageFeatureSet* function. The log10 value of genes per unique molecular identifier was  
 204 calculated as log10(number of genes) / log10(number of oligonucleotides). Initially the median  
 205 value of mitochondrial read percentage was determined, and maximum and minimum thresholds  
 206 were set at +3 and -3 times median absolute deviation (MAD), respectively. The same procedure  
 207 was applied to the log10 values of number of genes detected. Additionally, the +3 MAD was used  
 208 to define only the maximum threshold for log10(number of oligonucleotides) values. This  
 209 automated filtering process was applied to each sample individually.

210

$$211 \text{median}(x) = \begin{cases} X \left\lfloor \frac{n+1}{2} \right\rfloor & \text{if } n \text{ is odd} \\ X \left\lfloor \frac{n}{2} \right\rfloor + X \left\lfloor \frac{n}{2} + 1 \right\rfloor & \text{if } n \text{ is even} \end{cases}$$

212

$$213 \text{MAD} = \text{median}(|x - \text{median}(x)|)$$

214

215        *Mitochondrial Content(thresholds)*  
216            = median(mitochondrial gene%)  $\pm 3 \times MAD(mitochondrial gene\%)$   
217  
218        *Expression Profile(thresholds)* 1) median( $\log_{10} nFeature$ )  $\pm 3 \times MAD(\log_{10} nFeature)$ ,  
2) median( $\log_{10} nCount$ ) + 3  $\times MAD(\log_{10} nCount)$

219  
220  
221         $\chi$  = Feature of the ST dataset  
222         $n$  = number of the values in the feature dataset  
223         $nFeature$  = Number of gene captured  
224         $nCount$  = Number of oligonucleotide captured  
225

226        The data was visualized with ggplot2 (version 3.5.0) and ggExtra (version 0.10.1) to confirm the  
227 filtering criteria.

228  
229 **Visium ST data processing**  
230

231        Filtered spots were normalized using the *SCTransform*<sup>91</sup> function in *Seurat* (version 5.0.3).<sup>92</sup> The  
232 top 5,000 variable genes were then identified using the variance stabilizing transformation method  
233 through the *FindVariableFeatures* function. Subsequently, principal component analysis of the  
234 spots was performed using the *RunPCA* function. Uniform Manifold Approximation and Projection  
235 (UMAP) layouts and nearest-neighbor graphs were generated using the top 25 components.  
236 Different resolutions for spatial clustering were explored to determine the optimal resolution for  
237 analyzing tissue structure. Each sample's data were stored as *Seurat* objects.  
238

239 **Spatial spot deconvolution of BM with scRNA-seq reference dataset**  
240

241        Single-cell RNA sequencing (scRNA-seq) *Seurat* objects, predefined for cell types and stored as  
242 RDS files, were loaded using the *readRDS* function. Cells from 9 healthy BM samples ( $n = 62,862$   
243 cells) and the AML cells subset from 7 patients with diploid karyotype BM ( $n = 16,167$  cells) were  
244 integrated using the *merge* function. The combined dataset was then normalized with  
245 *SCTransform*, and the top 2,500 features were identified using *FindVariableFeatures*. A total of  
246 79,029 cells were scaled and centered using the *ScaleData* function. Dimensional reduction was  
247 performed on the scaled data with principal component analysis (PCA) using the *RunPCA*  
248 function, selecting 50 principal components with assigning *npcs* parameter as 50. Batch effects  
249 potentially arising from this integration were removed using the *RunHarmony* function from the  
250 *Harmony* package.<sup>93</sup> Neighborhoods and clusters were computed using the top 30 principal  
251 components, followed by calculation of UMAP layouts.

252  
253        To deconvolve cell types in spatial spots utilizing predefined cell-type labels from the reference  
254 scRNA-seq dataset, transfer learning was employed using the *Seurat* package. Integration  
255 anchors between the ST data and the scRNA-seq reference were established using the

256 *FindTransferAnchors* function, employing SCT normalization. During this alignment, residuals  
257 were not recomputed, as specified by setting the *recompute.residuals* parameter to False.

258  
259 Following anchor identification, cell-type annotations were transferred from the scRNA-seq  
260 dataset to the ST data using the *TransferData* function. This function applies a weighted nearest  
261 neighbor approach, leveraging weights derived from the first 25 principal components of the PCA  
262 embeddings specific to the ST data. The annotations transferred in this manner were stored in a  
263 new assay within the ST dataset.

264  
265 To further categorize the spatial spots, deconvolution scores from the assigned cell-types were  
266 used. Spots with AML prediction scores above the median value (median = 0.15) were classified  
267 as AML-enriched, while those below this threshold were designated as AML-depleted. For  
268 detailed deconvolution AML-enriched spots were subsetted. Only AML cells from our scRNA-seq  
269 data, along with predefined AML cell state information, were used to deconvolve AML cell  
270 populations within the AML-enriched spots using the same transfer learning approach.

271  
272 **Spatial spot deconvolution of EM samples**

273  
274 EM sample data stored as Seurat objects were converted to *SpaCET* objects using the  
275 *convert.Seurat* function from the *SpaCET* package (version 1.1.0).<sup>38</sup> The *SpaCET.deconvolution*  
276 function was then used to deconvolve these data using the Pan Cancer dictionary, which includes  
277 average all cancer type-specific expression signatures for 30 solid tumors, with the *cancerType*  
278 parameter set to 'PANCAN'. To identify malignant states within our tissues, the  
279 *SpaCET.deconvolution.malignant* function was used. The deconvolution results were added to  
280 the EM samples' Seurat object as a new assay using the *addTo.Seurat* function. Subsequently,  
281 these scores were visualized and assessed using the *SpatialFeaturePlot* in Seurat package.

282  
283 In the EM1 sample, the leukemic population within the cluster 1 was isolated using the *subset*  
284 function. Subsequently, similar to our approach with the BM1 sample, the AML cell population  
285 and their corresponding cell state information present in our scRNA-seq dataset were specifically  
286 deconvolved using a transfer learning approach.

287  
288 **Spatial Co-Localization Analysis**

289  
290 Deconvolution scores for leukemic populations were used to define spots with high and low  
291 leukemic scores in BM. Deconvolution scores that contain all cellular composition information  
292 were stored as a new assay in the BM2' Seurat object. Wilcoxon rank sum test applied to define  
293 differential scores of cell types with the *RunDEtest* function from the SCP (version 0.5.1) package.  
294 Results were visualized with the VolcanoPlot function.

295  
296 In EM, deconvolution scores were extracted from the Seurat object. The scores were then  
297 transposed, and a Pearson correlation matrix was calculated to evaluate the pairwise correlation

298 between cell type abundances. Mean deconvolution was computed to determine the abundance  
299 of each cell type.

300

### 301 **Spatial Cell-Cell Communication Analysis**

302

303 Cell labels were assigned to spots based on prediction probabilities from a custom function  
304 *assignLabels*. The data was prepared for cell-cell communication analysis using the CellChat  
305 package<sup>46</sup> (version 2.1.2), with spatial locations and conversion factors obtained from the 10X  
306 Visium data. A CellChat object was created with *createCellChat* function, and ligand-receptor  
307 interaction databases were set and subsetted using *subsetDB* to focus on secreted signaling.  
308 Overexpressed genes and interactions were identified with *identifyOverExpressedGenes* and  
309 *identifyOverExpressedInteractions*.

310

311 Communication probabilities were computed using *computeCommunProb*, and the cell-cell  
312 communication network was inferred. Pathway analysis was performed with  
313 *computeCommunProbPathway*, *netAnalysis\_computeCentrality*, and  
314 *netAnalysis\_signalingRole\_network*. Specific pathways such as CXCL highlighted using  
315 *netVisual\_* functions and *plotGeneExpression*.

316

### 317 **SpatialTime and Distance Analysis**

318

319 SpatialTime analysis was performed following established methods.<sup>51,94</sup> Initially, contours were  
320 manually drawn on Visium CytAssist image of trabecula with ImageJ2 (version 2.14.0). For each  
321 spatial spot in the BM, distances to the closest contoured surface were computed and scaled from  
322 0 (adjacent to the surface) to 1 (furthest from the surface). The median of the calculated  
323 SpatialTime values was used to define proximity and distality: spots above this calculations  
324 median value (median = 0.15) were classified as distal, while those below it were classified as  
325 proximal. Deconvolution results were visualized using the *FeatureStatPlot* function of the R  
326 package *SCP* to display the concentration of features at different distances relative to the  
327 trabeculae.

328

### 329 **Pathway Analysis and Inflammation Classification**

330

331 Pathway analysis was conducted using curated gene sets (hallmark), obtained from the Molecular  
332 Signatures Database (MSigDB). These gene sets were individually scored for each sample using  
333 the AUCell<sup>95</sup> (version 1.24.0) pipeline, and the resulting scores were integrated into our datasets.

334

335 Spatial coordinates and pathway scores for inflammatory pathways were extracted from the  
336 Seurat objects including inflammatory response, IL6/JAK/STAT3 signaling, IFNy Response, IFN $\alpha$   
337 Response, TNF $\alpha$ /NF- $\kappa$ B signaling, complement, and IL2/STAT5 signaling. Pathway scores were  
338 normalized to a 0-1 scale, and a composite score was calculated as the mean of these normalized  
339 scores. Coordinates and composite scores were combined into a data frame, and Jenks Natural

340 Breaks method was applied to categorize composite scores into four categories: Low, Medium-  
341 Low, Medium-High, and High. A spatial map was created to visualize composite inflammatory  
342 pathway activity. Box plots were generated to compare composite scores across related  
343 classification (Clusters, CXCL12-CXCR4, PI3K/AKT/mTOR, Trans-differentiation). Composite  
344 scores and classes were added to the Seurat object's metadata, ensuring alignment with the  
345 spots in the object. Spatial feature and dimension plots were generated to visualize composite  
346 scores and categories within the spatial context of the tissue sections.  
347

## 348 **Results**

### 349 **Comparative spatial transcriptomics analysis of BM and EM tissues in AML**

350

351 Trehine BM biopsies from two AML patients, along with a cutaneous myeloid sarcoma (skin)  
352 punch biopsy (EM1) from patient 1 (PT1) and a surgical biopsy of a mediastinal lymph node EM  
353 mass (EM2) from patient 2 (PT2), were collected at the time of AML diagnosis (pre-treatment)  
354 and were used for Visium-based ST profiling (**Figure 1A**). Clinical characteristics of these patients  
355 are summarized in **Table S1**. Briefly, PT1 (age 41 years; male) developed cutaneous myeloid  
356 sarcoma with concomitant medullary (BM) leukemia, characterized by 30% myeloblasts in the BM  
357 (BM1). PT2 (age 83 years; male) presented with a mediastinal mass but showed no  
358 histopathologic confirmation of medullary involvement of his AML (2% myeloblasts detected in  
359 BM2) (**Figure S1A-C**). While the targeted mutation panel in EM2 was negative for mutations, the  
360 BM of PT1 revealed mutations in *NPM1*, *DNMT3A*, *IDH1*, *IDH2*, *FLT3*, *SF3B1*, and *KRAS*. Both  
361 patients' BM samples had diploid cytogenetics.  
362

363 RNA fragmentation before Visium library preparation (pre-library), measured as the percentage  
364 of fragments > 200 nucleotides (DV<sub>200</sub>), varied across the 4 analyzed samples (range 24-62%;  
365 mean DV<sub>200</sub> = 44.5, standard deviation = 16.6) (**Figure 1B**, **Figure S1D**). The EM2 sample  
366 showed the lowest pre-library DV<sub>200</sub> value at 24%, whereas the BM2 sample from the same patient  
367 displayed the highest pre-library DV<sub>200</sub> metric at 62%. Then, to compare the assays and prepare  
368 the libraries for ST profiling, we used two Visium-based assays; version 1 (v1) (direct placement  
369 of each tissue section on a spatially-barcoded Visium slide), and version 2 (v2) (utilizes a tissue  
370 transfer-based approach in the CytAssist instrument) on all 4 patient samples in parallel, totaling  
371 8 libraries. For BM tissues, post-library DNA traces for v1 libraries were markedly lower compared  
372 to v2 (24% and 29% for v1 versus 89% and 91% for BM1 and BM2, respectively) (**Figure 1C**,  
373 **Figure S1E, F**), precluding further sequencing of v1 BM libraries. However, for EM tissues, the  
374 post-library DNA tracing was similar between v1 and v2 (EM1: 87% and EM2: 83% for v1, and  
375 EM1: 88% and EM2: 91% for v2). This suggests that Visium v2 automated tissue transfer provides  
376 a more reliable performance compared to v1, even with low pre-library DV<sub>200</sub> measures.  
377

378 Spatial mapping of oligonucleotide and gene counts obtained by SpaceRanger pipeline revealed  
379 that compared to v1, v2 assay had more oligonucleotides detected (mean nCount; 1292.76 for v1  
380 vs 11072.37 for v2) and genes identified (mean nFeature; 955.19 for v1 vs 4735.67 for v2) per  
381 sample (**Figure 1D**; **Figures S1G-I**). As expected, the median oligonucleotides detected and  
382 genes identified were positively correlated ( $r = 0.996$ ,  $p = 1.4 \times 10^{-5}$ ) (**Figure S1J**). Mitochondrial

383 gene percentages, available for v2 only, were highest in EM2, consistent with a necrotic  
384 phenotype on the histopathologic assessment (**Figure S1B**). Of note, prelib DV<sub>200</sub> values were  
385 negatively correlated with the median percentage of mitochondrial genes detected ( $r = -0.838$ ;  $p$   
386 = 0.1625) (**Figure S1L**). These mitochondrial reads were higher at the edge of the samples  
387 (**Figure S1K**). To assess whether the structural integrity of bone regions was maintained during  
388 tissue processing, we overlaid the hematoxylin and eosin (H&E) image generated on the same  
389 Visium slide of BM tissues with the ST data derived from SpaceRanger. Indeed, spots in bone  
390 trabeculae areas that usually have low cell abundance and tendency to come off during tissue  
391 processing were still maintained (**Figure 1E**, **Figure S1M**), allowing downstream analysis of  
392 spatial BM components using the CytAssist transfer-based approach.  
393

#### 394 **Spatial clustering and spot deconvolution reveal tissue morphology**

395

396 To our knowledge, Visium-based approaches in AML is not explored. This is particularly pertinent  
397 due to decalcification, RNA quality and unique bone-rich environment of AML compared to solid  
398 cancers. We thus adapted the median absolute deviation (MAD) on the spot level quality metrics  
399 to filter spots based on the normal distribution of mitochondrial content and expression profile  
400 (**Methods**, **Figure S2A-F**). To spatially delineate spot-level cellular information, we then  
401 deconvolved individual spots using probabilistic label transfer workflow<sup>33</sup> based on our in-house  
402 generated scRNA BM reference (**Figure 2A**). This reference map consisted of 79,029 cells  
403 collected from 9 healthy BM donors and 7 patients with AML with diploid cytogenetics including  
404 both newly generated scRNA data and previous works.<sup>13,34</sup> The reference map was clustered into  
405 a total of 21 different cell types, including T cells (CD4<sup>+</sup> and CD8<sup>+</sup> naïve, effector, and memory T  
406 cells, T regulatory [Treg] cells, and unconventional T cells), other immune cells (Natural killer [NK]  
407 cells, B cells and plasma cells), hematopoietic progenitors (Hematopoietic stem cells [HSCs],  
408 common lymphoid progenitors [CLPs], granulocyte-monocyte progenitors [GMPs]), myeloid cells  
409 (megakaryocytes/platelets, monocytes, early and late erythroid cells, conventional and  
410 plasmacytoid dendritic cells) and leukemic (AML) cell populations. The identities of these cell  
411 types were verified using canonical gene expression, as previously done.<sup>13,34-36</sup>  
412

413 We next performed shared nearest neighbor (SNN) modularity optimization<sup>37</sup> based unsupervised  
414 clustering and compared the cluster profiling to hematopathologist-identified histopathologic  
415 tissue annotation i.e. ground truth (**Figure 2B**, **Figure S3B-D**). For instance, in BM1,  
416 unsupervised clustering segmented the BM into 3 distinct clusters. Independently, the pathologist  
417 also identified 3 distinct regions with an adjusted rand index (ARI) of 0.46 (demonstrating  
418 moderate overlap). Further, regions 1, 2 and 3 were annotated by the pathologist as mixed,  
419 erythroid-enriched and monocytic/leukemia-enriched, respectively, which was consistent with the  
420 deconvolution analysis (**Figure 2C**, **Figure S3E**). To further validate the deconvolution-derived  
421 spot annotation, images stained with H&E, CD11c, CD3 and myeloperoxidase (MPO) on serial  
422 slides imaged, overlaid with the Visium slides and were evaluated by a hematopathologist (**Figure**  
423 **S3A,F**). This was further supported by differential expressed gene analysis and canonical  
424 markers on ST data of these regions by erythroid cells (*HBB*, *HBA2*, *GATA1*, *GATA2*), monocytes  
425 (*S100A12*, *FCGR3A*, *CD14*, *MS4A7*), and early myeloid cells (*CD33*) (**Figure 2D**, **Table S2**). We

426 detected all 21/21 (100%) of the cell types in our reference map. In BM1, the most abundant cell  
427 type was AML with late erythroid cells and monocytes, whereas in BM2 it was late erythroid cells  
428 with GMPs were most common (**Figure S3G**). Compared to BM2 (no leukemia detected), BM1  
429 (~30% leukemic blasts) had slightly higher prevalence of effector and memory T-cell populations,  
430 while BM2 had high abundance of erythroid-lineage populations (**Figure 2E**).  
431

432 Since EM tissues are non-medullary tissues and contains tissues such as epidermis, dermis,  
433 germinal centers, glands, etc., we applied the Spatial Cellular Estimator for Tumors (SpaCET)  
434 algorithm<sup>38</sup> optimized for solid non-BM cancers to identify tumor regions (**Methods**).  
435 Unsupervised clustering segmented the tissue into 3 distinct regions, which mostly overlapped  
436 with histopathological annotations except that of glandular tissue ( $ARI = 0.51$ ) (**Figure 2F**).  
437 Similar to our approach in BM samples, deconvolution results were confirmed with the  
438 histopathologic annotations using the same-slide H&E digital images (**Figure 2G, Figure S3A**).  
439 In EM1, macrophages were the predominant cell population, whereas cancer-associated  
440 fibroblasts and endothelial cells were the most enriched in EM2 (**Figure S3H**). Tissue-specific  
441 markers and differential expressed genes validated transcriptional segregation, revealing dermis  
442 infiltration by leukemic cells in EM1, and confirmed the consistency of unsupervised clusters with  
443 pathologist-defined regions (**Figure 2H, Figure S3I, Table S3**). These results support our use of  
444 deconvolution for spot-level annotation allowing further downstream analysis.  
445

#### 446 **AML-population focused analysis demonstrates spatial heterogeneity by cell 447 compositions in both BM and EM tissues**

  
448

449 Using the median deconvolution score, we assigned spots as high leukemic scores (HLS) (greater  
450 than the median of 0.15) or low leukemic scores (LLS) (**Figure 3A**). In BM1, cluster-based  
451 zonation revealed that HLS spots were ~14% more abundant in cluster 3, while LLS spots  
452 exhibited a 20% increase in cluster 2 (**Figure 3B**). GMPs and monocytes were both localized in  
453 HLS spots, with monocytes predominantly in cluster 3 and GMPs scattered across clusters  
454 (**Figure 3C, D**). CD8<sup>+</sup> naive cells were scattered throughout, with a higher concentration in cluster  
455 1, which contained mixed cell populations (**Figure 3E**). Spots harboring late erythroid cells were  
456 predominantly found in the cluster 2 where HLS spots were least abundant (22.9% of HLS spots)  
457 and encompassed the most LLS spots (42.9% of LLS spots). In EM1, immune cell populations  
458 were found to be localized together within the tissue. Notably, macrophages, which had the  
459 highest abundance in EM1, showed strong co-localization with classical dendritic cells (*Pearson*  
460 *correlation coefficient (r) = 0.67*) and significant associations with cancer-associated fibroblasts (*r*  
461 = 0.37) (**Figure 3F**). Spatial mapping revealed that macrophages and classical dendritic cells co-  
462 localized in regions with tumor infiltration in the dermis (**Figure 3G**). These results revealed that  
463 GMPs and monocytes co-localize with leukemic-enriched populations in the BM, while  
464 macrophages are concentrated in tumor-infiltrated regions in the EM.  
465

#### 466 **Inferred pathway and cell communication analysis uncover interaction of CXCL12-CXCR4 467 axis with inflammation**

  
468

469 Differential gene expression analysis was conducted on HLS spots relative to LLS spots in BM1  
470 (**Figure S4A, TableS4**). We discovered that genes highly expressed in HLS-spots were  
471 concentrated in cluster 3 (**Figure S4B**). Among these genes associated with leukemic regions in  
472 the BM, those such as *CD70*,<sup>39</sup> *TMEM176B*,<sup>40,41</sup> *TP53INP2*,<sup>42</sup> and *TNFSF13B*,<sup>43</sup> which are  
473 associated with immune regulation and tumor progression, were also found to be expressed in  
474 the leukemic regions of the same patient's EM sample (**Figure 4A**).  
475

476 Interestingly, pathway profiling revealed the concomitant BM and EM samples of same patients  
477 also displayed similar molecular signatures (**Figure S4C**), suggesting similar biologic programs  
478 governing medullary and EM leukemia. For instance, in BM1, pathways related to inflammation  
479 (IFN $\alpha$ , IFN $\gamma$ , inflammatory response, and TGF- $\beta$ ), and energy metabolism (oxidative-  
480 phosphorylation [OXPHOS] and glycolysis), were upregulated in both sample of PT1 but were  
481 slightly downregulated in the samples from PT2. Additionally, epithelial-mesenchymal transition  
482 (EMT)-like signatures linked to neoplastic cell migration and trans-differentiation were prominent  
483 in our EM samples. Comparing pathway activities between spatial clusters within each tissue, we  
484 found a similar profiles between cluster 3 of BM1 and the leukemic population cluster of EM1  
485 (**Figure S4D**).  
486

487 Dysregulated inflammatory pathways in the BM microenvironment contribute to leukemogenesis  
488 and leukemic blast maintenance in AML.<sup>44,45</sup> To identify the inflammation niche in our AML-  
489 affected BM sample (BM1), we defined a composite inflammation score using inflammation-  
490 related hallmark pathways (inflammatory response, IL6/JAK/STAT3 signaling, IFN $\alpha$  and IFN $\gamma$ ,  
491 response, TNF $\alpha$  signaling via NF- $\kappa$ B, complement, and IL2/STAT5 signaling) and then clustered  
492 the spatial data using Jenks natural breaks optimization (**Methods, Figure 4B**). We observed a  
493 high inflammation profile in BM1 that was concentrated in cluster 3, mirroring the high  
494 inflammation scores found in the leukemic population of EM1 (**Figure S4E,F**). Further, we found  
495 that the hypoxic environment (Hypoxia, reactive oxygen species and HIF1A pathways) intensified  
496 within the highly inflammatory niche (**Figure S4G**). Taken together, our findings demonstrate that  
497 the leukemic population in distinct tissues from the same patient can exhibit similar biologic  
498 profiles.  
499

500 We then evaluated the spatial cell-cell interactions.<sup>46</sup> Based on deconvolution results; each spot  
501 was labeled according to the cell type with the maximum prediction probability (**Figure S5A**). Our  
502 analysis revealed that CXCL pathways between annotated spots exhibited the highest signaling  
503 strength (**Figure S5B**). Specifically, the CXCL12-CXCR4 axis showed that monocytes and GMPs  
504 co-localized with AML cells in HLS spots (**Figure 3C-D**), indicating communication through this  
505 pathway (**Figure 4C, Figure S5C-D**). Examining the relationship of the CXCL12-CXCR4 pair  
506 within the inflammatory niche, we found that both the CXCL12 ligand and the CXCR4 receptor  
507 showed high expression levels in medium-high and high inflammation spots in BM1 (**Figure 4D**).  
508

509 The PI3K/AKT/mTOR pathway, a downstream target of these chemokines, was highly correlated  
510 with CXCL12-CXCR4 co-expression in regions of elevated inflammation (**Figure 4E, Figure**  
511 **S5E,F**).<sup>47</sup> This pathway is also involved in the direct induction of trans-differentiation (**Figure**

512 **S5G**)<sup>48</sup> aligning with our findings of elevated EMT pathway in these regions. To understand the  
513 involvement of this PI3K/AKT/mTOR through CXCL12-CXCR4 pathway at the EM site, we  
514 examined the spatial expression profiles of its ligand-receptor communication. We observed that  
515 CXCR4 was abundantly expressed throughout the tissue and correlated with the composite  
516 inflammation score (**Figure 4F**). Additionally, the PI3K/AKT/mTOR pathway and trans-  
517 differentiation states were active in regions with high inflammation in EM (**Figure 4G, Figure**  
518 **S5H,I**). These observations suggest that leukemic populations in the BM concentrate within the  
519 inflammatory niche via CXCL12-CXCR4 chemokine signaling, activating trans-differentiation  
520 through the PI3K/AKT/mTOR pathway. Additionally, the elevated levels of CXCR4 and  
521 inflammation in EM suggest a possible path for medullary leukemia to migrate EM tissues.  
522

## 523 **Deconvolution of leukemic-enriched spots reveals the localization of different** 524 **differentiation states of AML cells within inflammatory and endosteal niches**

525  
526 We next applied linear mixed model annotation<sup>49</sup> to classify AML cells (n=16,167) from scRNA  
527 into their differentiation states relative to the hierarchies in healthy BM controls (n=20,778 cells).<sup>50</sup>  
528 This classification defined AML cells as: primitive-like (combination of HSC-like, common myeloid  
529 progenitor/lymphoid-primed multipotent progenitor-like; n= 5,039), GMP-like (n=6,432), erythroid-  
530 like (n= 1,816), lymphoid-like (n = 55), and committed-like (combination of monocyte-like,  
531 basophil-like, dendritic cell-like; n=2,825) (**Figure 5A**). We then applied this classification to BM  
532 HLS spots (n=1,271 spots) and EM1 leukemic-enriched spots (n = 1,726 spots) (**Figure 5B, C**)  
533 to obtain a spot-level classification of hierarchies. Cluster-based niches revealed that committed-  
534 like populations were located distally to the primitive-like populations (**Figure S6B, C**).  
535 Deconvolution scores indicated a lower abundance of primitive-like cells compared to committed-  
536 like cells in EM tissue (**Figure S6D,E**). We found that committed-like AML populations were  
537 concentrated in inflammatory niches in both BM and EM tissues (**Figure 5D,E**). We then applied  
538 the SpatialTime pipeline<sup>51</sup> (**Methods**) to measure the spatial localization of HLS spots relative to  
539 the trabecular bone regions and based on the degree of AML differentiation (**Figure 5F, Figure**  
540 **S6F**). We found that primitive-like cell populations were localized proximally to the bone, while  
541 GMP- and committed-like populations were localized distally (**Figure 5G**). To validate these  
542 findings, we performed a GeoMx-based whole-transcriptome microdissection-based assay also  
543 known as digital spatial profiling (DSP) on 13 BM regions from 3 independent newly diagnosed  
544 AML patients (mean age: 73 years; 3 male). (**Figure S6G-H**). CD34 and CD68 protein markers  
545 were used to define the leukemic regions covering primitive and more differentiated cells (**Figure**  
546 **S6I-J**). Congruent with our Visium ST analysis, phenotypically primitive-like cells were detected  
547 proximal to the bone, while more differentiated cell states were predominantly found in regions  
548 distal from the bone (**Figure 5H, I**). Taken together, these findings suggest that AML cells at  
549 different states of differentiation locate in distinct niches within the BM.

550  
551 **Discussion**  
552  
553 Understanding AML microenvironments requires unveiling the spatial niches along the medullary-  
554 extramedullary leukemia axis and the interactions between myeloid neoplastic populations and

555 the immune system. Spatial transcriptomics (ST) technologies offer valuable insights but face  
556 challenges in BM-centric diseases due to preservation issues.<sup>52,53</sup> In this study, we mapped  
557 human BM and EM tissues exhibiting the presence of AML using decalcified and archived core  
558 biopsy tissues, revealing significant interactions within the CXCL12-CXCR4 axis. This mapping  
559 highlights AML populations' spatial localizations in various differentiation states within endosteal  
560 and inflammatory niches. Additionally, we validated these findings using GeoMX DSP and  
561 identified the most applicable Visium-based ST assays for leukemic tissues.

562

563 Inflammation is one of the hallmarks of cancer.<sup>54</sup> Recent studies have shown that inflammatory  
564 states alter the immune microenvironment and are driven by specific differentiation stages in  
565 AML.<sup>13,55–57</sup> These inflammatory microenvironments play roles in the maintenance of leukemic  
566 populations, disease progression, and chemoresistance.<sup>58,59</sup> Here, inflammatory classification of  
567 spatial spots revealed niches in both AML-affected BM and EM leukemia. Although these  
568 inflammation niches harbored AML cells at various differentiation states, there was a strong  
569 association between a more committed-like phenotype and inflammation. The inflammation-high  
570 niches also created a hypoxic environment, linked to reactive oxygen species production and HIF  
571 pathway activation.<sup>60</sup> Importantly, hypoxic microenvironments create protective niches that  
572 mediate resistance to therapy.<sup>61</sup>

573

574 Notably, we found that the inflammation niche was strongly associated with the region enriched  
575 for AML and monocytes, which communicate strongly through the CXCL12-CXCR4 axis.  
576 CXCL12, which is also a target of HIF-1 $\alpha$ <sup>62</sup>, binds to CXC chemokine receptor 4 (CXCR4), a G-  
577 protein-coupled chemokine receptor, essential for the interaction between AML cells and the BM  
578 stroma. This interaction contributes to myeloid neoplastic progression, cell homing, and  
579 migration<sup>63–66</sup> and has been studied as a therapeutic target in leukemia.<sup>67–69</sup> CXCR4 mediates  
580 chemotaxis and retention of cells within the BM niche by interacting with the CXCL12 gradient.<sup>70</sup>  
581 This axis is also thought to play a role in EM acute lymphoblastic leukemia and AML infiltration,  
582 with particularly higher expression levels identified in AML-M4/M5 subtypes.<sup>71–73</sup> Here, we showed  
583 that spatial CXCR4 expression is highly abundant and widespread in EM tissue. Therefore,  
584 consistent with previous studies, it is possible that CXCR4 is not only a homing factor for the BM  
585 but also facilitates the migration and homing of leukemia populations to EM sites.

586

587 CXCR4 has previously been implicated in EMT-like transcriptional activation in EM disease in  
588 multiple myeloma.<sup>74</sup> The PI3K/Akt/mTOR pathway is one of the downstream targets of the  
589 CXCL12-CXCR4 axis and is recognized as an important regulator of EMT in solid tumors, playing  
590 a crucial role in tumor cell migration and metastasis.<sup>47,48,75,76</sup> In AML, this EMT-like pathway, which  
591 we refer to as a trans-differentiation state, shows correlation with the PI3K/Akt/mTOR pathway in  
592 inflammatory niches with high CXCL12-CXCR4 signaling. Targeting the CXCL12-CXCR4-  
593 enriched inflammatory niche may therefore reduce trans-differentiation and the development of  
594 leukemia cutis, offering potential benefits for patients with concurrent medullary and  
595 extramedullary AML.

596

597 The AML population in the BM exhibited a transcriptional profile similar to that of EM leukemia  
598 within this inflammatory niche, revealing both common and specific genes and pathways for  
599 spatial niche analysis. Beyond the previously identified chimeric antigen receptor (CAR)-T therapy  
600 target, *CD70*,<sup>77,78</sup> we observed the upregulation of genes such as *RAB3D*,<sup>79</sup> associated with  
601 monocytic AML subtypes, and *TP53/NP2*,<sup>42,80</sup> linked to autophagy activity in NPM1-mutated AML,  
602 within these regions. Additionally, the high expression of *TNFSF13B* and *TMEM176B*, markers  
603 not yet definitively linked to AML, in regions populated by monocyte-like AML populations and in  
604 corresponding EM leukemia areas, highlights the need for further research on these markers for  
605 prognosis and as potential therapeutic targets.

606

607 The interaction between hematopoiesis and the endosteal niche in the BM is crucial for  
608 maintaining HSC quiescence, self-renewal, and differentiation; facilitating HSC homing and  
609 mobilization, and supporting the BM microenvironment.<sup>81,82</sup> Previous studies have shown that  
610 HSCs and multipotent progenitors are closely associated with the bone surface in the endosteal  
611 region, whereas committed progenitors and differentiated cells are positioned more distally.<sup>83–86</sup>  
612 Additionally, a comprehensive spatial atlas of the human BM niche has been provided by cellular  
613 biogeography mapping studies.<sup>87</sup> Here, we extended prior findings by examining spatial  
614 interactions in BM with AML. The differentiation states of AML cells are challenging to define using  
615 individual markers. We provided a new approach to examine the connection between AML  
616 populations at distinct differentiation states and the endosteal niche in BM tissues using  
617 multimodal spatial transcriptomic analysis. Our findings suggest that while leukemic populations  
618 in the GMP and committed differentiation states are located further from the endosteal niche,  
619 primitive-like cells are in closer proximity. This suggests that leukemic cell maintenance and  
620 stemness are supported by this niche.

621

622 In summary, our study provides a comprehensive ST analysis of medullary and EM tissues in  
623 AML using multimodal ST technologies. We identified distinct inflammatory niches in both BM and  
624 EM samples, with significant involvement of the CXCL12-CXCR4 axis. This axis promotes trans-  
625 differentation via the PI3K/AKT/mTOR pathway, contributing to AML cell migration and infiltration  
626 into EM sites. Spatial analysis revealed that primitive-like AML cells are predominantly located  
627 near the endosteal niche in BM, while committed-like and GMP-like populations are situated more  
628 distally. These findings highlight the critical role of inflammatory niches in AML progression and  
629 provide novel insights into leukemic cell spatial heterogeneity, underscoring potential targets for  
630 therapeutic intervention.

631

### 632 **Limitations of the study**

633

634 Our study presents one of the initial spatial analyses at the RNA level along the human medullary-  
635 extramedullary leukemia axis, yet is limited by the number of samples. This is due in part to the  
636 cost-prohibitive nature of these assays (Visium and DSP). Nevertheless, our study represents the  
637 first study evaluating the spatial dynamics of medullary and EM leukemia in paired patient  
638 samples constituting a very rare sample population, which will serve as a resource for other  
639 researchers. Additionally, the 55-μm spot-based structure of Visium ST technology leads to low

640 resolution in tissues like BM, which have highly heterogeneous cellular compositions. To  
641 overcome this limitation, we have implemented several strategies: (i) We adapted a MAD-based  
642 filtering method specific to each tissue structure to identify spots with outlier reads. (ii) We defined  
643 intra-sample niches using broader range clusters. (iii) We validated cell prediction results with  
644 pathology annotations made using both H&E and immunohistochemical analysis. (iv) We  
645 validated the Visium results using DSP for higher resolution.

646

#### 647 **Resource availability**

648

649 All data from this will be publicly available via an interactive webportal (video provided with this  
650 submission) for other researchers to navigate. All codes will be publicly available on.

651

#### 652 **Data Availability**

653

654 Spatial transcriptomics data will be publicly available at GEO as of the date of publication.  
655 Additionally, an interactive web application will be launched concurrently, allowing researchers to  
656 explore the data interactively.

657

#### 658 **Acknowledgements**

659

660 We would like to thank Sarah Bronson at the Research Medical Library and Thomas Huynh and  
661 Arizona Nguyen at the Department of Veterinary Services, and Dr. Chong Wu at the Department  
662 of Biostatistics at The University of Texas MD Anderson Cancer Center. HAA was funded by the  
663 Physician Scientist Award and CPRIT.

664

#### 665 **Conflicts of interests**

666

667 H.A.A. received research support from Illumina. P.S. received private investment from Adaptive  
668 Biotechnologies, BioNTech, JSL Health, Sporos, and Time Bioventures and served as scientific  
669 advisory committee member for Achelois, Affini-T, Akoya Biosciences, Apricity, Asher Bio, BioAtla  
670 LLC, Candel Therapeutics, Catalio, C-Reveal Therapeutics, Dragonfly Therapeutics, Earli Inc,  
671 Enable Medicine, Glympse, Henlius/Hengenix, Hummingbird, ImaginAb, InterVenn Biosciences,  
672 LAVA Therapeutics, Lytix Biopharma, Marker Therapeutics, Matrisome, Oncolytics, Osteologic,  
673 PBM Capital, Phenomic AI, Polaris Pharma, Spotlight, Trained Therapeutix Discovery, Two Bear  
674 Capital, and Xilis, Inc.. All other authors declare no relevant conflict of interest.

675

#### 676 **Contributions**

677

678 H.A.A. conceived the study, supervised all aspects of the work, co-wrote and reviewed the  
679 manuscript. E.D., I.V. and H.A.A. wrote the manuscript. E.D. led the computational analyses and  
680 interpretation of Visium data. I.V. and C.P.L. analyzed DSP data. A.E.Q. and F.Z.J. performed  
681 pathology annotations. P.B., S.B., S.J., Z.W., A.L., and K.M.W. conducted the experiments and/or

682 library preparation. D.A.A., P.H.G., P.K.R. and R.J.T., contributed conceptually to data analysis  
683 and design. All authors read and edited the manuscript.

684

685

686 **References**

687

688 1. Döhner, H., Weisdorf, D. J. & Bloomfield, C. D. Acute Myeloid Leukemia. *N. Engl. J. Med.* **373**,  
689 1136–1152 (2015).

690 2. Ishii, H. & Yano, S. New Therapeutic Strategies for Adult Acute Myeloid Leukemia. *Cancers*  
691 **14**, 2806 (2022).

692 3. Bhansali, R. S., Pratz, K. W. & Lai, C. Recent advances in targeted therapies in acute myeloid  
693 leukemia. *J. Hematol. Oncol.* **16**, 29 (2023).

694 4. Siegel, R. L., Miller, K. D., Fuchs, H. E. & Jemal, A. Cancer statistics, 2022. *CA: A Cancer J.*  
695 *Clin.* **72**, 7–33 (2022).

696 5. Austin, R., Smyth, M. J. & Lane, S. W. Harnessing the immune system in acute myeloid  
697 leukaemia. *Crit. Rev. Oncol.Hematol.* **103**, 62–77 (2016).

698 6. Khalidyanidi, S., Nagorsen, D., Stein, A., Ossenkoppele, G. & Subklewe, M. Immune Biology  
699 of Acute Myeloid Leukemia: Implications for Immunotherapy. *J. Clin. Oncol.* **39**, 419–432 (2021).

700 7. Stölzel, F. *et al.* The prevalence of extramedullary acute myeloid leukemia detected by 18FDG-  
701 PET/CT: final results from the prospective PETAML trial. *Haematologica* **105**, 1552–1558 (2020).

702 8. Abbas, H. A. *et al.* Clinical and molecular characterization of myeloid sarcoma without  
703 medullary leukemia. *Leuk. Lymphoma* **62**, 3402–3410 (2021).

704 9. Galen, P. van *et al.* Single-Cell RNA-Seq Reveals AML Hierarchies Relevant to Disease  
705 Progression and Immunity. *Cell* **176**, 1265–1281.e24 (2019).

706 10. Ediriwickrema, A., Gentles, A. J. & Majeti, R. Single-cell genomics in AML: extending the  
707 frontiers of AML research. *Blood* **141**, 345–355 (2023).

708 11. Tikhonova, A. N. *et al.* The bone marrow microenvironment at single-cell resolution. *Nature*  
709 **569**, 222–228 (2019).

710 12. Ben-Chetrit, N. *et al.* Integration of whole transcriptome spatial profiling with protein markers.  
711 *Nat. Biotechnol.* **41**, 788–793 (2023).

712 13. Wang, B. *et al.* Comprehensive characterization of IFNy signaling in acute myeloid leukemia  
713 reveals prognostic and therapeutic strategies. *Nat. Commun.* **15**, 1821 (2024).

- 714 14. Lamble, A. J. & Lind, E. F. Targeting the Immune Microenvironment in Acute Myeloid  
715 Leukemia: A Focus on T Cell Immunity. *Front. Oncol.* **8**, 213 (2018).
- 716 15. Emdal, K. B. *et al.* Phosphoproteomics of primary AML patient samples reveals rationale for  
717 AKT combination therapy and p53 context to overcome selinexor resistance. *Cell Rep.* **40**,  
718 111177 (2022).
- 719 16. Williams, C. G., Lee, H. J., Asatsuma, T., Vento-Tormo, R. & Haque, A. An introduction to  
720 spatial transcriptomics for biomedical research. *Genome Med.* **14**, 68 (2022).
- 721 17. Method of the Year 2020: spatially resolved transcriptomics. *Nat. Methods* **18**, 1–1 (2021).
- 722 18. Crosetto, N., Bienko, M. & Oudenaarden, A. van. Spatially resolved transcriptomics and  
723 beyond. *Nat. Rev. Genet.* **16**, 57–66 (2015).
- 724 19. Satija, R., Farrell, J. A., Gennert, D., Schier, A. F. & Regev, A. Spatial reconstruction of single-  
725 cell gene expression data. *Nat. Biotechnol.* **33**, 495–502 (2015).
- 726 20. Moses, L. & Pachter, L. Museum of spatial transcriptomics. *Nat. Methods* **19**, 534–546 (2022).
- 727 21. Asp, M., Bergenstråhle, J. & Lundeberg, J. Spatially Resolved Transcriptomes—Next  
728 Generation Tools for Tissue Exploration. *BioEssays* **42**, e1900221 (2020).
- 729 22. Dong, R. & Yuan, G.-C. SpatialDWLS: accurate deconvolution of spatial transcriptomic data.  
730 *Genome Biol.* **22**, 145 (2021).
- 731 23. Elosua-Bayes, M., Nieto, P., Mereu, E., Gut, I. & Heyn, H. SPOTlight: seeded NMF regression  
732 to deconvolute spatial transcriptomics spots with single-cell transcriptomes. *Nucleic Acids Res.*  
733 **49**, e50–e50 (2021).
- 734 24. Cable, D. M. *et al.* Robust decomposition of cell type mixtures in spatial transcriptomics. *Nat.*  
735 *Biotechnol.* **40**, 517–526 (2022).
- 736 25. Andersson, A. *et al.* Single-cell and spatial transcriptomics enables probabilistic inference of  
737 cell type topography. *Commun. Biol.* **3**, 565 (2020).
- 738 26. Vahid, M. R. *et al.* High-resolution alignment of single-cell and spatial transcriptomes with  
739 CytoSPACE. *Nat. Biotechnol.* **41**, 1543–1548 (2023).
- 740 27. Kleshchevnikov, V. *et al.* Cell2location maps fine-grained cell types in spatial transcriptomics.  
741 *Nat. Biotechnol.* **40**, 661–671 (2022).
- 742 28. Maynard, K. R. *et al.* Transcriptome-scale spatial gene expression in the human dorsolateral  
743 prefrontal cortex. *Nat. Neurosci.* **24**, 425–436 (2021).
- 744 29. Hunter, M. V., Moncada, R., Weiss, J. M., Yanai, I. & White, R. M. Spatially resolved  
745 transcriptomics reveals the architecture of the tumor-microenvironment interface. *Nat. Commun.*  
746 **12**, 6278 (2021).

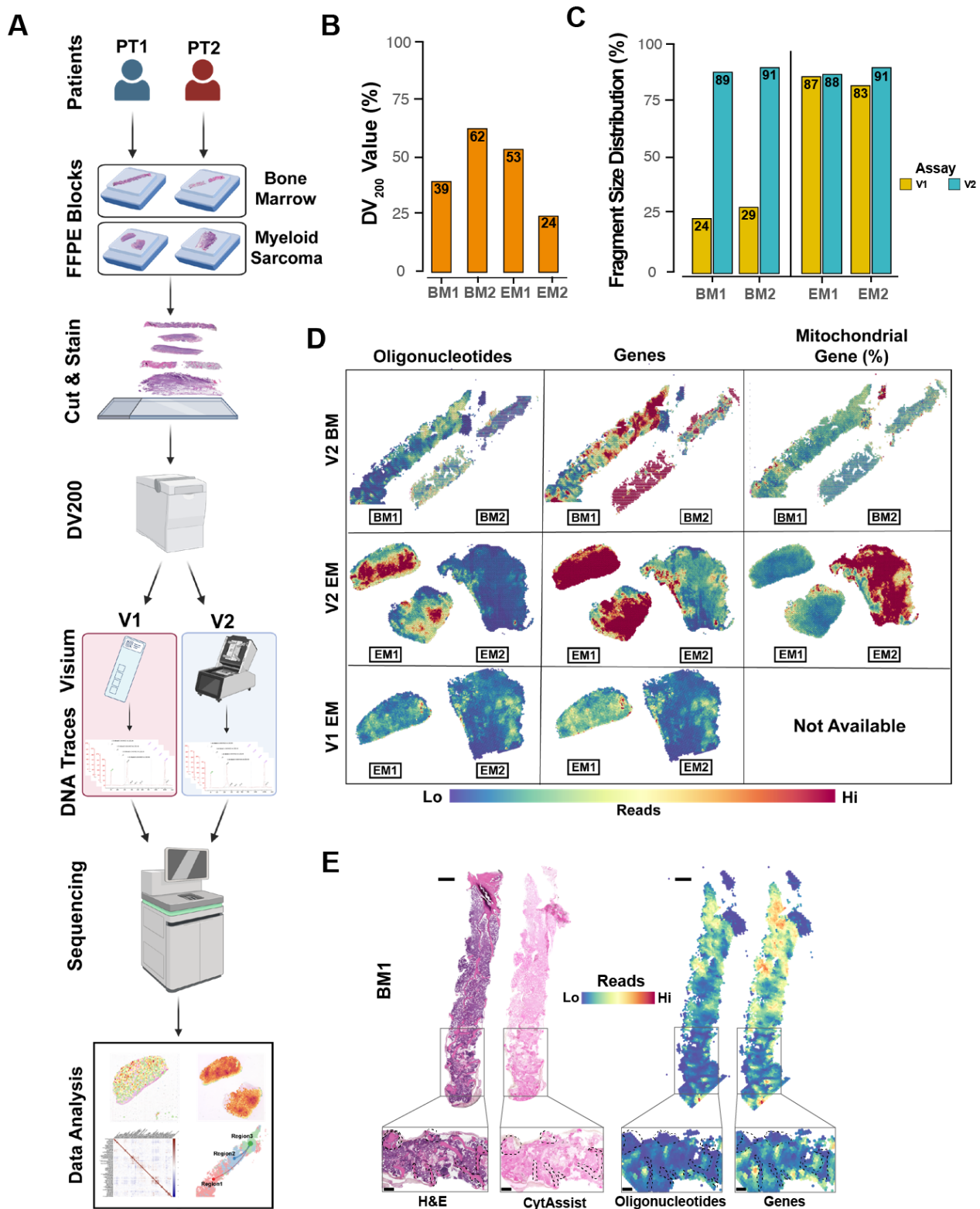
- 747 30. Ferreira, R. M. *et al.* Integration of spatial and single cell transcriptomics localizes epithelial-  
748 immune cross-talk in kidney injury. *JCI Insight* **6**, e147703 (2021).
- 749 31. Kim, S. *et al.* Integrative analysis of spatial and single-cell transcriptome data from human  
750 pancreatic cancer reveals an intermediate cancer cell population associated with poor prognosis.  
751 *Genome Med.* **16**, 20 (2024).
- 752 32. Cohen, C. *et al.* WNT-dependent interaction between inflammatory fibroblasts and FOLR2+  
753 macrophages promotes fibrosis in chronic kidney disease. *Nat. Commun.* **15**, 743 (2024).
- 754 33. Stuart, T. *et al.* Comprehensive Integration of Single-Cell Data. *Cell* **177**, 1888-1902.e21  
755 (2019).
- 756 34. Desai, P. N. *et al.* Single-Cell Profiling of CD8+ T Cells in Acute Myeloid Leukemia Reveals a  
757 Continuous Spectrum of Differentiation and Clonal Hyperexpansion. *Cancer Immunol. Res.* **11**,  
758 1011–1028 (2023).
- 759 35. Abbas, H. A. *et al.* Single cell T cell landscape and T cell receptor repertoire profiling of AML  
760 in context of PD-1 blockade therapy. *Nat. Commun.* **12**, 6071 (2021).
- 761 36. Rutella, S. *et al.* Signatures of immune dysfunction predict outcomes and define checkpoint  
762 blockade-unresponsive microenvironments in acute myeloid leukemia. *J. Clin. Investig.* **132**,  
763 e159579 (2022).
- 764 37. Waltman, L. & Eck, N. J. van. A smart local moving algorithm for large-scale modularity-based  
765 community detection. *Eur. Phys. J. B* **86**, 471 (2013).
- 766 38. Ru, B., Huang, J., Zhang, Y., Aldape, K. & Jiang, P. Estimation of cell lineages in tumors from  
767 spatial transcriptomics data. *Nat. Commun.* **14**, 568 (2023).
- 768 39. Riether, C. *et al.* Targeting CD70 with cusatuzumab eliminates acute myeloid leukemia stem  
769 cells in patients treated with hypomethylating agents. *Nat. Med.* **26**, 1459–1467 (2020).
- 770 40. Segovia, M. *et al.* Targeting TMEM176B Enhances Antitumor Immunity and Augments the  
771 Efficacy of Immune Checkpoint Blockers by Unleashing Inflammasome Activation. *Cancer Cell*  
772 **35**, 767-781.e6 (2019).
- 773 41. Li, J. *et al.* Transmembrane protein 176B regulates amino acid metabolism through the PI3K-  
774 Akt-mTOR signaling pathway and promotes gastric cancer progression. *Cancer Cell Int.* **24**, 95  
775 (2024).
- 776 42. Huang, J. *et al.* Cytoplasmic Expression of TP53INP2 Modulated by Demethylase FTO and  
777 Mutant NPM1 Promotes Autophagy in Leukemia Cells. *Int. J. Mol. Sci.* **24**, 1624 (2023).
- 778 43. Chapellier, M. *et al.* Arrayed molecular barcoding identifies TNFSF13 as a positive regulator  
779 of acute myeloid leukemia-initiating cells. *Haematologica* **104**, 2006–2016 (2019).

- 780 44. Chen, L. *et al.* A SINGLE-CELL TAXONOMY PREDICTS INFLAMMATORY NICHE  
781 REMODELING TO DRIVE TISSUE FAILURE AND OUTCOME IN HUMAN AML. *Blood Cancer*  
782 *Discov.* **4**, 394–417 (2023).
- 783 45. Zambetti, N. A. *et al.* Mesenchymal Inflammation Drives Genotoxic Stress in Hematopoietic  
784 Stem Cells and Predicts Disease Evolution in Human Pre-leukemia. *Cell Stem Cell* **19**, 613–627  
785 (2016).
- 786 46. Jin, S., Plikus, M. V. & Nie, Q. CellChat for systematic analysis of cell-cell communication  
787 from single-cell and spatially resolved transcriptomics. *bioRxiv* 2023.11.05.565674 (2023)  
788 doi:10.1101/2023.11.05.565674.
- 789 47. Cancilla, D., Rettig, M. P. & DiPersio, J. F. Targeting CXCR4 in AML and ALL. *Front. Oncol.*  
790 **10**, 1672 (2020).
- 791 48. Xu, W., Yang, Z. & Lu, N. A new role for the PI3K/Akt signaling pathway in the epithelial-  
792 mesenchymal transition. *Cell Adhes. Migr.* **9**, 317–324 (2015).
- 793 49. Kang, J. B. *et al.* Efficient and precise single-cell reference atlas mapping with Symphony.  
794 *Nat. Commun.* **12**, 5890 (2021).
- 795 50. Granja, J. M. *et al.* Single-cell multiomic analysis identifies regulatory programs in mixed-  
796 phenotype acute leukemia. *Nat. Biotechnol.* **37**, 1458–1465 (2019).
- 797 51. Tower, R. J. *et al.* Spatial transcriptomics reveals a role for sensory nerves in preserving  
798 cranial suture patency through modulation of BMP/TGF- $\beta$  signaling. *Proc. Natl. Acad. Sci.* **118**,  
799 e2103087118 (2021).
- 800 52. Singh, V. M. *et al.* Analysis of the effect of various decalcification agents on the quantity and  
801 quality of nucleic acid (DNA and RNA) recovered from bone biopsies. *Ann. Diagn. Pathol.* **17**,  
802 322–326 (2013).
- 803 53. Fang, S. *et al.* Computational Approaches and Challenges in Spatial Transcriptomics.  
804 *Genom., Proteom. Bioinform.* **21**, 24–47 (2022).
- 805 54. Hanahan, D. & Weinberg, R. A. Hallmarks of Cancer: The Next Generation. *Cell* **144**, 646–  
806 674 (2011).
- 807 55. Lasry, A. *et al.* An inflammatory state remodels the immune microenvironment and improves  
808 risk stratification in acute myeloid leukemia. *Nat. Cancer* **4**, 27–42 (2023).
- 809 56. Vadakekolathu, J. *et al.* Immune landscapes predict chemotherapy resistance and  
810 immunotherapy response in acute myeloid leukemia. *Sci. Transl. Med.* **12**, (2020).
- 811 57. Corradi, G. *et al.* Release of IFNy by Acute Myeloid Leukemia Cells Remodels Bone Marrow  
812 Immune Microenvironment by Inducing Regulatory T Cells. *Clin. Cancer Res.* **28**, 3141–3155  
813 (2022).

- 814 58. Ellegast, J. M. *et al.* Unleashing cell-intrinsic inflammation as a strategy to kill AML blasts Cell-  
815 intrinsic inflammation as a strategy to kill AML blasts. *Cancer Discov.* **12**, 1760–1781 (2022).
- 816 59. Récher, C. Clinical Implications of Inflammation in Acute Myeloid Leukemia. *Front. Oncol.* **11**,  
817 623952 (2021).
- 818 60. Fuhrmann, D. C. & Brüne, B. Mitochondrial composition and function under the control of  
819 hypoxia. *Redox Biol.* **12**, 208–215 (2017).
- 820 61. Bruno, S. *et al.* The Role of Hypoxic Bone Marrow Microenvironment in Acute Myeloid  
821 Leukemia and Future Therapeutic Opportunities. *Int. J. Mol. Sci.* **22**, 6857 (2021).
- 822 62. Fiegl, M. *et al.* CXCR4 expression and biologic activity in acute myeloid leukemia are  
823 dependent on oxygen partial pressure. *Blood* **113**, 1504–1512 (2009).
- 824 63. Ayala, F., Dewar, R., Kieran, M. & Kalluri, R. Contribution of bone microenvironment to  
825 leukemogenesis and leukemia progression. *Leukemia* **23**, 2233–2241 (2009).
- 826 64. Braun, M. *et al.* CXCL12 promotes glycolytic reprogramming in acute myeloid leukemia cells  
827 via the CXCR4/mTOR axis. *Leukemia* **30**, 1788–1792 (2016).
- 828 65. Ladikou, E. E., Chevassut, T., Pepper, C. J. & Pepper, A. G. Dissecting the role of the  
829 CXCL12/CXCR4 axis in acute myeloid leukaemia. *Br. J. Haematol.* **189**, 815–825 (2020).
- 830 66. Tavor, S. *et al.* CXCR4 Regulates Migration and Development of Human Acute Myelogenous  
831 Leukemia Stem Cells in Transplanted NOD/SCID Mice. *Cancer Res.* **64**, 2817–2824 (2004).
- 832 67. Yang, P., Hu, Y. & Zhou, Q. The CXCL12-CXCR4 Signaling Axis Plays a Key Role in Cancer  
833 Metastasis and is a Potential Target for Developing Novel Therapeutics against Metastatic  
834 Cancer. *Curr. Med. Chem.* **27**, 5543–5561 (2019).
- 835 68. Cho, B.-S., Kim, H.-J. & Konopleva, M. Targeting the CXCL12/CXCR4 axis in acute myeloid  
836 leukemia: from bench to bedside. *Korean J. Intern. Med.* **32**, 248–257 (2017).
- 837 69. Abraham, M. *et al.* The CXCR4 inhibitor BL-8040 induces the apoptosis of AML blasts by  
838 downregulating ERK, BCL-2, MCL-1 and cyclin-D1 via altered miR-15a/16-1 expression.  
839 *Leukemia* **31**, 2336–2346 (2017).
- 840 70. Sugiyama, T., Kohara, H., Noda, M. & Nagasawa, T. Maintenance of the Hematopoietic Stem  
841 Cell Pool by CXCL12-CXCR4 Chemokine Signaling in Bone Marrow Stromal Cell Niches.  
842 *Immunity* **25**, 977–988 (2006).
- 843 71. Du, W. *et al.* Prognostic significance of CXCR4 expression in acute myeloid leukemia. *Cancer  
844 Med.* **8**, 6595–6603 (2019).
- 845 72. Cazzolara, R. *et al.* High expression of the chemokine receptor CXCR4 predicts  
846 extramedullary organ infiltration in childhood acute lymphoblastic leukaemia. *Br. J. Haematol.*  
847 **115**, 545–553 (2001).

- 848 73. Zhang, Y. *et al.* CXCR4 inhibitors selectively eliminate CXCR4-expressing human acute  
849 myeloid leukemia cells in NOG mouse model. *Cell Death Dis.* **3**, e396–e396 (2012).
- 850 74. Roccaro, A. M. *et al.* CXCR4 Regulates Extra-Medullary Myeloma through Epithelial-  
851 Mesenchymal-Transition-like Transcriptional Activation. *Cell Rep.* **12**, 622–635 (2015).
- 852 75. Maharati, A. & Moghbeli, M. PI3K/AKT signaling pathway as a critical regulator of epithelial-  
853 mesenchymal transition in colorectal tumor cells. *Cell Commun. Signal.* **21**, 201 (2023).
- 854 76. Roshan, M. K. *et al.* Role of AKT and mTOR signaling pathways in the induction of epithelial-  
855 mesenchymal transition (EMT) process. *Biochimie* **165**, 229–234 (2019).
- 856 77. Wu, G. *et al.* Preclinical evaluation of CD70-specific CAR T cells targeting acute myeloid  
857 leukemia. *Front. Immunol.* **14**, 1093750 (2023).
- 858 78. Wang, X., Zhang, Y. & Xue, S. Recent progress in chimeric antigen receptor therapy for acute  
859 myeloid leukemia. *Ann. Hematol.* 1–15 (2024) doi:10.1007/s00277-023-05601-y.
- 860 79. Liu, J. *et al.* RAB3D/MDM2/β-catenin/c-MYC axis exacerbates the malignant behaviors of  
861 acute myeloid leukemia cells in vitro and in vivo. *Cancer Gene Ther.* **30**, 335–344 (2023).
- 862 80. Zou, Q. *et al.* NPM1 Mutant Mediated PML Delocalization and Stabilization Enhances  
863 Autophagy and Cell Survival in Leukemic Cells. *Theranostics* **7**, 2289–2304 (2017).
- 864 81. Fröbel, J. *et al.* The Hematopoietic Bone Marrow Niche Ecosystem. *Front. Cell Dev. Biol.* **9**,  
865 705410 (2021).
- 866 82. Lévesque, J.-P., Helwani, F. M. & Winkler, I. G. The endosteal ‘osteoblastic’ niche and its role  
867 in hematopoietic stem cell homing and mobilization. *Leukemia* **24**, 1979–1992 (2010).
- 868 83. Lord, B. I., Testa, N. G. & Hendry, J. H. The Relative Spatial Distributions of CFUs and CFUc  
869 in the Normal Mouse Femur. *Blood* **46**, 65–72 (1975).
- 870 84. Taichman, R. S. & Emerson, S. G. Human osteoblasts support hematopoiesis through the  
871 production of granulocyte colony-stimulating factor. *J. Exp. Med.* **179**, 1677–1682 (1994).
- 872 85. Nilsson, S. K., Johnston, H. M. & Coverdale, J. A. Spatial localization of transplanted  
873 hemopoietic stem cells: inferences for the localization of stem cell niches. *Blood* **97**, 2293–2299  
874 (2001).
- 875 86. Cordeiro-Spinetti, E., Taichman, R. S. & Balduino, A. The Bone Marrow Endosteal Niche:  
876 How Far from the Surface? *J. Cell. Biochem.* **116**, 6–11 (2015).
- 877 87. Bandyopadhyay, S. *et al.* Mapping the cellular biogeography of human bone marrow niches  
878 using single-cell transcriptomics and proteomic imaging. *Cell* (2024)  
879 doi:10.1016/j.cell.2024.04.013.
- 880 88. MAN-10154-01-GeoMx-DSP-Data-Analysis-User-Manual.pdf. <https://nanostring.com/wp-content/uploads/2022/06/MAN-10154-01-GeoMx-DSP-Data-Analysis-User-Manual.pdf>.

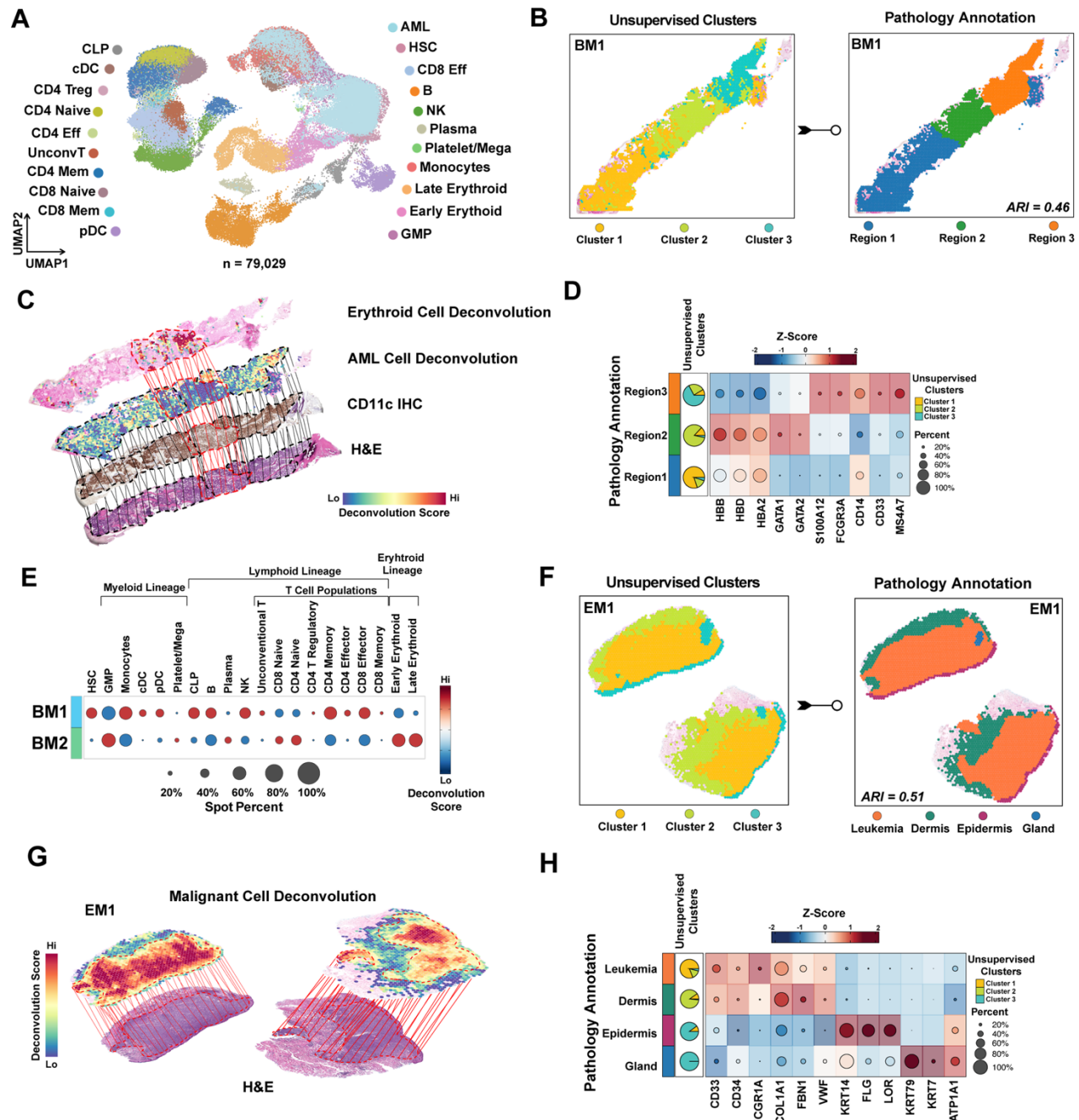
- 882 89. Griswold, M., Ortogero, N., Yang, Z., Vitancol, R. & Henderson, D. GeomxTools.  
883 <https://bioconductor.org/packages/release/bioc/html/GeomxTools.html> (2021).
- 884 90. Newman, A. M. *et al.* Determining cell type abundance and expression from bulk tissues with  
885 digital cytometry. *Nat. Biotechnol.* **37**, 773–782 (2019).
- 886 91. Hafemeister, C. & Satija, R. Normalization and variance stabilization of single-cell RNA-seq  
887 data using regularized negative binomial regression. *Genome Biol.* **20**, 296 (2019).
- 888 92. Hao, Y. *et al.* Dictionary learning for integrative, multimodal and scalable single-cell analysis.  
889 *Nat. Biotechnol.* **42**, 293–304 (2024).
- 890 93. Korsunsky, I. *et al.* Fast, sensitive and accurate integration of single-cell data with Harmony.  
891 *Nat. Methods* **16**, 1289–1296 (2019).
- 892 94. Xiao, X. *et al.* Spatial transcriptomic interrogation of the murine bone marrow signaling  
893 landscape. *Bone Res.* **11**, 59 (2023).
- 894 95. Aibar, S. *et al.* SCENIC: single-cell regulatory network inference and clustering. *Nat. Methods*  
895 **14**, 1083–1086 (2017).
- 896 96. Khoury, J.D., Solary, E., Abla, O., Akkari, Y., Alaggio, R., Apperley, J.F., Bejar, R., Berti, E.,  
897 Busque, L., Chan, J.K.C., et al. (2022). The 5th edition of the World Health Organization  
898 Classification of Haematolymphoid Tumours: Myeloid and Histiocytic/Dendritic Neoplasms.  
899 *Leukemia* **36**, 1703–1719. <https://doi.org/10.1038/s41375-022-01613-1>.
- 900 97. Döhner, H., Wei, A.H., Appelbaum, F.R., Craddock, C., DiNardo, C.D., Dombret, H., Ebert,  
901 B.L., Fenaux, P., Godley, L.A., Hasserjian, R.P., et al. (2022). Diagnosis and management of AML  
902 in adults: 2022 recommendations from an international expert panel on behalf of the ELN. *Blood*  
903 **140**, 1345–1377. <https://doi.org/10.1182/blood.2022016867>.
- 904 98. Ok, C.Y., Singh, R., Luthra, R., Hatfield, D., Floyd, K., Loghavi, S., Kanagal-Shamanna, R.,  
905 Zuo, Z., Yin, C.C., Routbort, M., et al. (2017). Endleukemia Assay v1: Enabling NGS-Based  
906 Comprehensive Routine Molecular Profiling of Leukemias in Routine Clinical Care. **130**, 2679–  
907 2679. [https://doi.org/10.1182/blood.v130.suppl\\_1.2679.2679](https://doi.org/10.1182/blood.v130.suppl_1.2679.2679).
- 908  
909  
910



913 **Figure 1: Study overview and Quality control comparison of Visium v1 and Visium v2.**

914

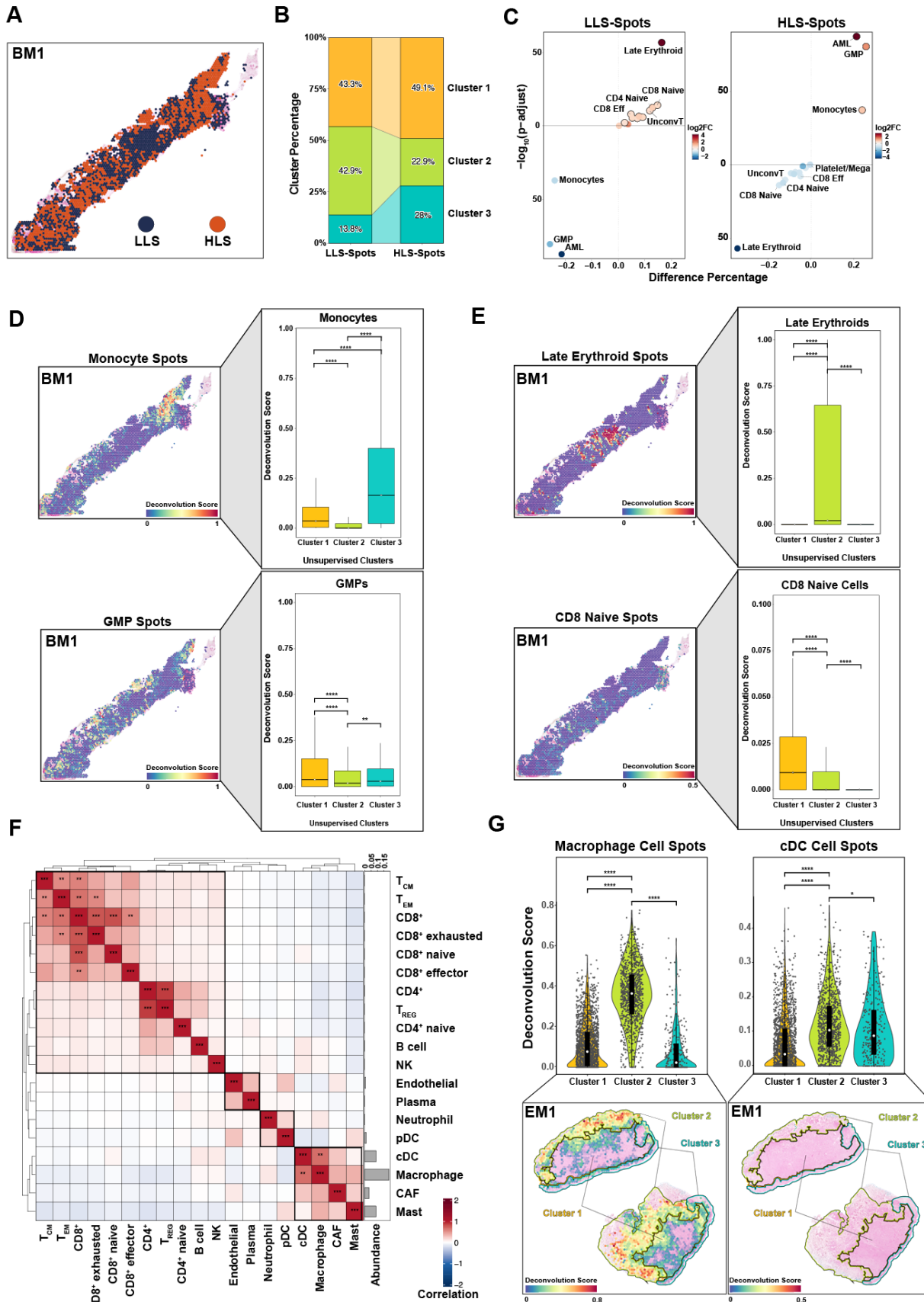
915 (A) Schematic representation of the study workflow, visualized by BioRender  
916 (<https://biorender.com/>). Concurrent Bone Marrow (BM) and Extramedullary (EM) (EM1 from skin  
917 and EM2 from lymph node) formalin-fixed paraffin-embedded samples from 2 newly diagnosed  
918 patients with acute myeloid leukemia (AML) (PT1 and PT2) were obtained. Each sample was  
919 sectioned and stained with hematoxylin and eosin (H&E). RNA integrity was evaluated using  
920 DV<sub>200</sub> measurements before library preparation. Visium ST assays v1 and CytAssist v2 were  
921 performed on each sample. After library preparation, cDNA traces were assessed, and samples  
922 meeting the criteria were sequenced for further analysis. (B) DV<sub>200</sub> values for BM1, BM2, EM1,  
923 and EM2 tissues, indicating RNA integrity before library preparation (C) Fragment size distribution  
924 percentages calculated within the 200-1000 bp range for DNA libraries prepared using v1 and v2  
925 assays. BM samples showed significant improvement with v2 compared to v1. EM samples were  
926 within the acceptable range for both assays. (D) Spatial mapping by Seurat of captured  
927 oligonucleotides, genes, and mitochondrial gene percentages in BM and EM tissues. The v2  
928 assay demonstrated higher oligonucleotide and gene capturing compared to v1, with  
929 mitochondrial gene percentages available only for v2. (E) Histological overlay of H&E-stained  
930 BM1 section with CytAssist image and spatial transcriptomics data, The image shows preserved  
931 structural integrity of bone regions, allowing detailed spatial analysis. The main tissue scale bar  
932 indicating 1 mm, while the zoomed-in panels, highlighting the boxed regions, denoting 400 µm.



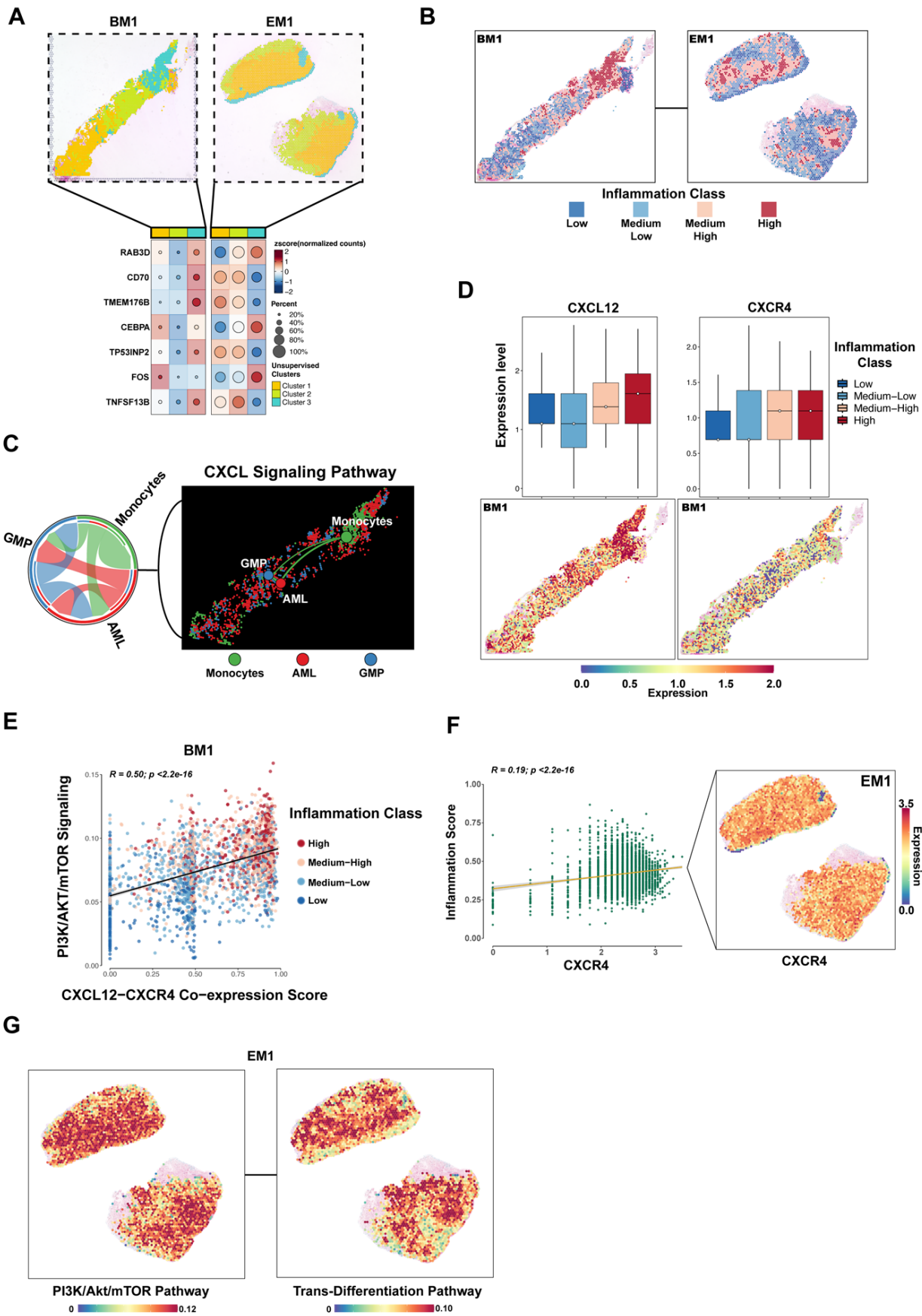
936 **Figure 2: Spatial clustering and cell deconvolution in AML tissues.**

938 **(A)** Uniform Manifold Approximation and Projection (UMAP) plot showing 21 different cell types  
939 identified from the scRNA reference map, derived from 79,029 cells from 9 healthy donors and 7  
940 diploid AML patients. AML, acute myeloid leukemia; cDC, classical dendritic cells; CLP, common  
941 lymphoid progenitors; Eff, effector T cells; GMP, granulocyte-monocyte progenitors; HSC,  
942 hematopoietic stem cells; Mega, megakaryocytes; Mem, memory T cells; NK, natural killer cells;

943 pDC, plasmacytoid dendritic cells; Treg, T regulatory cells; UnconvT, unconventional T cells. **(B)**  
944 Unsupervised clustering and pathology annotation for BM1 projected spatial map, revealing 3  
945 distinct regions with an adjusted Rand index (ARI) of 0.46. **(C)** Spatial deconvolution of BM1  
946 tissue, showing erythroid and AML cell populations, with CD11c immunohistochemistry (IHC)  
947 overlaid on an H&E-stained image. Dotted red lines represent regions enriched for the erythroid  
948 cell population. Dotted black lines indicate regions enriched for the AML cell population. Solid  
949 lines represent regions that overlapped with other tissue sections. **(D)** Heatmap showing  
950 canonical marker expression in pathology annotations, with matching unsupervised cluster  
951 distribution represented as a pie chart. **(E)** Dot plot depicting the percentage and deconvolution  
952 score of each cell type in BM1 versus BM2 tissues. **(F)** Spatial map of unsupervised clusters and  
953 pathology annotation for EM1, with an ARI of 0.51, identifying distinct tissue regions. **(G)** Spatial  
954 deconvolution of EM1 tissue obtained from SpaCET algorithm, showing malignant cell distribution  
955 overlaid on the H&E image. **(H)** Heatmap of canonical marker expression in EM1 regions,  
956 validating transcriptional segregation and matching pathologist-defined regions. Markers for  
957 leukemic population and dermis regions show shared expression profiles. Unsupervised cluster  
958 overlap is represented as pie charts, with pathology annotation.

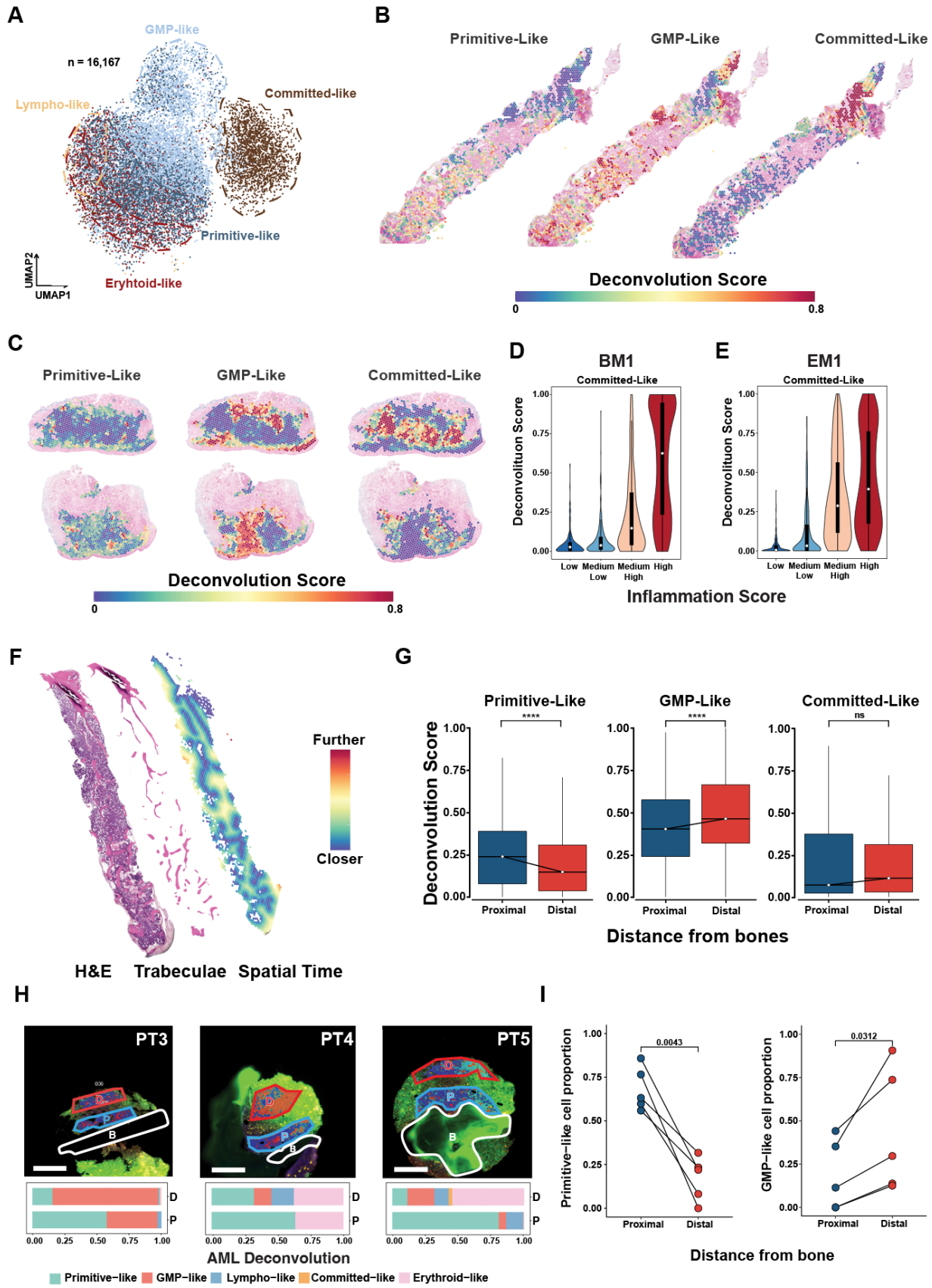


960 **Figure 3: Spatial heterogeneity of AML populations in BM and EM tissues.**  
961 **(A)** Spatial map of BM1 showing spots with high leukemic scores (HLS) (above median AML cells  
962 deconvolution score; >0.15) (orange) and low leukemic scores (LLS) (below median AML cells  
963 deconvolution score; <=0.15) (darkblue). **(B)** Stacked bar plot shows cluster-based distribution  
964 of HLS and LLS spots. **(C)** Volcano plot shows differential co-localization of cell populations within  
965 HLS and LLS spots. Deconvolution scores were compared by Wilcoxon rank sum test. **(D)** Spatial  
966 deconvolution and distribution (represented as a box plot) of monocytes and GMPs in HLS spots  
967 in BM1, with deconvolution scores indicating higher abundance in cluster 3. Median values are  
968 shown as white dots on a black line. **(E)** Spatial deconvolution and distribution of late erythroid  
969 cells and CD8 naïve cells in BM1, showing their localization in LLS spots. **(F)** Correlation heatmap  
970 of cell populations in EM1, highlighting significant co-localization between macrophages and  
971 classical dendritic cells (cDCs). Pearson absolute correlation: \*\*\*>0.7, \*\*>0.5. **(G)** Spatial mapping  
972 of macrophage and cDC spots in EM1, showing their co-localization in tumor-infiltrated dermis  
973 clusterd (clusters 1-2). \*p < 0.05, \*\*p < 0.01, \*\*\*p < 0.001, \*\*\*\*p < 0.0001, Wilcoxon rank sum test.



975 **Figure 4: Interaction of the CXCL12-CXCR4 axis with inflammation in AML tissues.**

976  
977 **(A)** The heatmap shows differential gene expression analysis of HLS spots relative to LLS spots  
978 in BM1, highlighting genes associated with immune regulation and tumor progression. Genes  
979 highly expressed in HLS spots of BM1, particularly in cluster 3, show a similar expression profile  
980 to that of the leukemic-enriched cluster 1 of EM1. **(B)** Spatial inflammation class distribution in  
981 BM1 and EM1, based on composite inflammation scores from inflammation-related hallmark  
982 pathways, shows medium-high and high inflammation spots concentrated in leukemic-enriched  
983 regions (cluster 3 in BM1 and cluster 1 in EM1). Classes were defined using Jenks natural breaks  
984 optimization. **(C)** Spatial and circus plot of AML-GMP-monocyte interactions and interactions  
985 strength among spots predicted by CellChat. **(D)** Box plots showing expression levels of CXCL12  
986 and CXCR4 in BM1, stratified by inflammation class. Spatial maps indicate expression  
987 distribution. **(E)** Correlation between PI3K/AKT/mTOR signaling and CXCL12-CXCR4 co-  
988 expression scores in BM1, stratified by inflammation class. T-distribution was used to evaluate  
989 the significance of Pearson correlation. **(F)** Relationship between CXCR4 expression and  
990 inflammation score in EM1, with spatial maps showing expression distribution. **(G)** Spatial  
991 mapping of PI3K/AKT/mTOR and trans-differentiation pathway (epithelial-mesenchymal transition  
992 from hallmark pathways) in EM1.



994 **Figure 5: Localization of AML cell differentiation states within inflammatory and endosteal**  
995 **niches**

996  
997 **(A)** UMAP projection of 16,167 AML cells into differentiation states: primitive-like, granulocyte-  
998 monocyte progenitor (GMP)-like, erythroid-like and lymphoid-like, and committed-like **(B)** Spatial  
999 deconvolution maps of HLS-spots of BM1 showing primitive-like, GMP-like, and committed-like  
1000 AML cells. **(C)** Spatial deconvolution maps of EM1 showing the same AML cell types. **(D, E)** Violin  
1001 plot showing the distribution of committed-like AML cells in BM1 **(D)**, and EM1 **(E)** across  
1002 inflammation class. **(F)** Spatial map of Spatial Time calculation according to trabeculae overlaid  
1003 with H&E image. **(G)** Box plots showing deconvolution scores of primitive-like, GMP-like, and  
1004 committed-like AML cells relative to their distance from bone in Visium data. Proximal is dark blue,  
1005 distal is dark red. **(H)** GeoMx analysis of AML deconvolution in bone marrow regions from 3 AML  
1006 patients. D: distal (dark red), P: proximal (dark blue), B:bone (white). Stacked bar plots represent  
1007 cell type deconvolution within distal and proximal regions. The scale bar is 250 $\mu$ m. **(I)** Line graphs  
1008 showing proportions of primitive-like and GMP-like cells relative to distance from bone.

1009 \*p < 0.05, \*\*p < 0.01, \*\*\*p < 0.001, \*\*\*\*p < 0.0001, Wilcoxon rank sum test.

1010

1011